



Considerations about the influence of the structural and electrochemical properties of carbonaceous materials on the behavior of lithium-ion capacitors



M. Schroeder^a, S. Menne^a, J. Ségalini^b, D. Saurel^b, M. Casas-Cabanas^b, S. Passerini^{a,c}, M. Winter^a, A. Balducci^{a,*}

^a Westfälische Wilhelms-Universität Münster, Institut für Physikalische Chemie-MEET, Corrensstraße 28/30, 48149 Münster, Germany

^b CIC Energigune, Parque Tecnológico, C/Albert Einstein 48, 01510 Miñano, Spain

^c Helmholtz Institute Ulm, Karlsruhe Institute of Technology, Albert Einstein Allee 11, Ulm, Germany

HIGHLIGHTS

- Lithium-ion capacitors are promising high power devices.
- Soft carbon is more suitable for application on LICs compared to graphite.
- Soft carbon-based lithium-ion capacitors display higher energy compared to graphite-based devices.

ARTICLE INFO

Article history:

Received 27 March 2014

Received in revised form

29 April 2014

Accepted 7 May 2014

Available online 16 May 2014

Keywords:

Lithium-ion capacitor

Soft carbon

Graphite

High power devices

ABSTRACT

Lithium-ion capacitors (LICs) have attracted an increased attention in the last years. Presently, graphite is the mostly used material for the negative electrodes of LICs. Nevertheless, many works showed that graphite electrodes display rather low performance during high rate charge, as those required for LICs. Therefore the use of alternative carbonaceous anodes could be of importance for the realization of advanced LICs. In this work we show that soft carbon represents a promising alternative to graphite. While the lithium insertion in graphite is hindered every time a new intercalation stage is reached, in soft carbon the lithium insertion process does not show significant decrease over the used potential range. This difference, caused by the different structural properties of these carbonaceous materials, has dramatic consequences on the capacity retention of these carbons during the high rates typically used in LICs.

© 2014 Elsevier B.V. All rights reserved.

1. Introduction

High power, hybrid devices have attracted an increased attention in the last years. These hybrid devices are realized combining a lithium-ion battery (LIB) electrode with a supercapacitor (SC) one [1–7]. Although many different combinations are possible, most of the recent publications focus on systems utilizing a LIB anode and activated carbon (AC) positive electrode. These devices are often addressed as lithium-ion capacitors (LICs).

The LIB anodes utilized in LICs can be divided into two main classes: lithium titanate and carbonaceous-based electrodes. The systems containing lithium titanate typically display high cycling

stability, they can be used with a broad range of electrolytes and they do not need particular preconditioning. However, since lithium is inserted and extracted at high potentials in these materials, e.g. 1.5 V vs. Li/Li⁺ in Li₄Ti₅O₁₂, the cell voltage of LICs containing them does not exceed 3 V [2,6,8–13]. Systems containing carbonaceous materials, on the other hand, display much higher cell voltage, in the order of 4 V, and consequently higher energy. This higher cell voltage can be reached due to the lower lithium insertion/extraction potential of these materials (down to 0 V vs. Li/Li⁺) compared to that of lithium titanate. However, this high cell voltage (in the range of LIBs) comes along with the formation of a solid electrolyte interphase (SEI) on the surface of the negative electrode. This effect has two important consequences: a LIB electrolyte, having SEI forming components (e.g. ethylene carbonate, EC), has to be chosen and the anode has to be precharged. Without precharging/prelithiation of the anode all lithium ions of the

* Corresponding author.

E-mail address: andrea.balducci@uni-muenster.de (A. Balducci).

electrolyte would be used to form the SEI and the cell would be useless after formation. Although the lithiation of the anode via the electrolyte has been proposed, additional metallic lithium is mostly considered as lithium ion source in LICs [14,15]. Commercial LICs use simply a metallic lithium foil, which is short circuited with the anode, while other publications propose the addition of stabilized lithium metal powder directly on top of the anode [16,17].

Similar to LIBs, LICs use mostly graphite as anode material both in academia and industry [14,15,17–21]. This selection appears somehow surprising, as many works showed that graphite displays rather low performance during high rate charge [20,21]. Although other carbonaceous materials like hard and soft carbons are used in high power LIBs, only a few articles considered their application in LICs [16,20,22–25]. In recent publications, we were able to show that soft carbon based LICs display high performance and that this material can be successfully used in combination with electrolytes, e.g. propylene carbonate or gel polymer electrolytes, displaying higher safety compared to the state-of-the-art electrolytes for LIBs [22,24]. The soft carbon used in this study, petroleum coke, has been widely characterized in the past and this material has been actually used in the negative electrode of the first commercialized LIB cells [26–31]. Nevertheless, it is interesting to note that basically all publications dedicated to this material focused on the analysis of its initial irreversible capacity and no detailed studies about the capacity retention at high currents have been reported.

In this manuscript we report a comparison of the morphological and structural characteristics as well as of the electrochemical properties of soft carbon and graphite electrodes. Two materials representative of each material class [21] have been selected and investigated in order to have a reliable comparison with regard to their use on LICs.

2. Experimental

All electrodes used in this work were prepared following a procedure similar to that described in literature [22]. As anode active materials petroleum coke PC-400C (PeC, Timcal, Switzerland, specific nitrogen BET surface area: $3.98 \text{ m}^2 \text{ g}^{-1}$, D90: $40 \mu\text{m}$) and synthetic flake graphite SFG6 (Timcal, Switzerland, specific BET area: $17 \text{ m}^2 \text{ g}^{-1}$, D90: $6.5 \mu\text{m}$) were used [32,33]. The active material for the positive activated carbon electrodes for the LIC full cell experiments was DLC Super 30 (AC, Norit, USA, specific BET surface area: $1400 \text{ m}^2 \text{ g}^{-1}$). Super C65 (Timcal, Switzerland) and sodium carboxymethylcellulose (CMC, Walocel CRT 2000 PA, Dow Wolff Cellulosics, Germany) were used in all electrodes as conductive agent and binder. The negative electrodes consisted of 90% active material, 5% conductive agent and 5% binder and had a mass loading of 1.9 mg cm^{-2} . The AC electrodes consisted of 80% active material, 15% conductive agent and 5% binder and had a mass loading of 2.9 mg cm^{-2} .

Both half and full cell tests were carried out in 3-electrode Swagelok®-type cells (electrode area 1.13 cm^2). The reference electrodes (and counter electrodes in half cell tests) were made of metallic lithium (Rockwood Lithium, Germany). The cell assembly was done in an argon filled glovebox (MBraun, Germany, H_2O and O_2 content < 1 ppm). The used electrolyte consisted of a mixture of 1 M LiPF₆ in EC:DMC 1:1 w:w (LP30, Selectlyte™, BASF, Germany).

The electrochemical experiments were performed in climatic chambers at 20°C either with a Maccor battery tester (Series 4000, Maccor Inc. USA, galvanostatic cycling, GITT measurements) or with a VMP multichannel potentiostatic–galvanostatic system (VMP, Biologic Science Instrument, France, cyclic voltammetries). Cyclic voltammetries were performed with a scan-rate of $50 \mu\text{V s}^{-1}$ in a potential range between 0.0 and $1.5 \text{ V vs. Li/Li}^+$. For the C-rate test, carried out using graphite and soft carbon electrodes, different

Table 1

Current densities applied during the charge–discharge tests carried out in half and full cells.

C-rate	$I_{\text{Half cell}}/\text{A g}^{-1}$	$I_{\text{Full cell}}/\text{A g}^{-1}$	$I/\text{mA cm}^{-2}$
1	0.372	0.15	0.66
5	1.9	0.74	3.3
15	5.6	2.2	9.9

rates were considered (C/10, C/5, C/2, 1C, C/5, 2.5C, 5C, C/5, 7.5C, 10C, C/5, 12.5C, 15C, C/5, 17.5C, 20C, C/5). For each C-rate, five cycles were carried out. The cells were cycled at C/5 after every two rates, to verify if the test was harming the electrodes. For clarity, only one cycle is shown in the C-rate plots. For GITT experiments, current pulses corresponding to C/10 were applied for ten minutes to the already formed anode before the cell had two hours time to relax. This procedure was repeated until a potential of $0.0 \text{ V vs. Li/Li}^+$ was under-cut. To determine the diffusion coefficient Eq. (1) is used. Included in this equation are τ as pulse period (600 s), m_B as active mass, M_B as molar mass (12 g mol^{-1}), V_m as molar Volume ($5.34 \text{ cm}^3 \text{ mol}^{-1}$), A as electroactive surface (derived from the geometric surface area of 1.13 cm^2) and L as the thickness of the electrode ($\sim 10 \mu\text{m}$). ΔE_S and ΔE_τ are the potential differences between the equilibrium potential and the excited potential before and after relaxation, respectively [34].

$$D_{\text{Li}^+} = \frac{4}{\pi \cdot \tau} \left(\frac{m_B \cdot V_m}{M_B \cdot A} \right)^2 \left(\frac{\Delta E_S}{\Delta E_\tau} \right)^2 \left(\tau \ll L^2 / D_{\text{Li}^+} \right) \quad (1)$$

The electrodes in the LIC full cells were prelithiated via the lithium reference electrode as described in literature [22]. Afterward, the LIC full cells were cycled between 0.0 and 4.0 V . A positive electrode discharge cut-off potential of $1.5 \text{ V vs. Li/Li}^+$ was added to prevent irreversible lithium insertion into the AC. The capacities and currents are based on the anode active mass in half cells and on both electrode active masses in full cells. The used currents are stated in Table 1.

In order to characterize the morphology of graphite and soft carbon High Resolution SEM micrographs were measured with an Auriga SEM (ZEISS, Germany). For structural characterization of the materials, Raman measurements were performed with a SENTERRA Dispersive Raman Microscope (Bruker, Germany, 732 nm laser wavelength, output power of 2 mW , four scans were performed). The diffractometer for powder XRD measurements (both *in-situ* and *ex-situ*) was a D8 Advance (Bruker, Germany, Cu-K α radiation $\lambda = 0.154 \text{ nm}$).

Electrochemical *in-situ* X-ray diffraction measurements were carried out using a 22 mm inner diameter electrochemical cell developed at CIC energiGUNE, equipped with a Be window as current collector, operating in reflection geometry. Pure powder PeC sample was cycled *in-situ* using lithium metal disk counter electrode and glass fiber separator (Whatman, GF/B) impregnated by LiPF₆ 1 M EC:DMC 1:1 electrolyte (Solvionic). The electrochemical cell was cycled at C/40 between 0.005 and 2 V using a SP200 Biologic potentiostat, with XRD patterns recorded every 30 min from 4 to 70° with a step of 0.03° .

SAXS measurements were performed using a Nanostar U (Bruker, Germany) equipped with microfocus Cu source, evacuated beam path and Vantec 2000 detector, using 107 cm and 13 cm sample-detector distances. The incident beam has been carefully calibrated in order to obtain absolute intensities in cm^{-1} with a perfect overlap of the measurements made at the two distances. Intensities were then normalized in $\text{cm}^2 \text{ g}^{-1}$ by the macroscopic density of the powder samples.

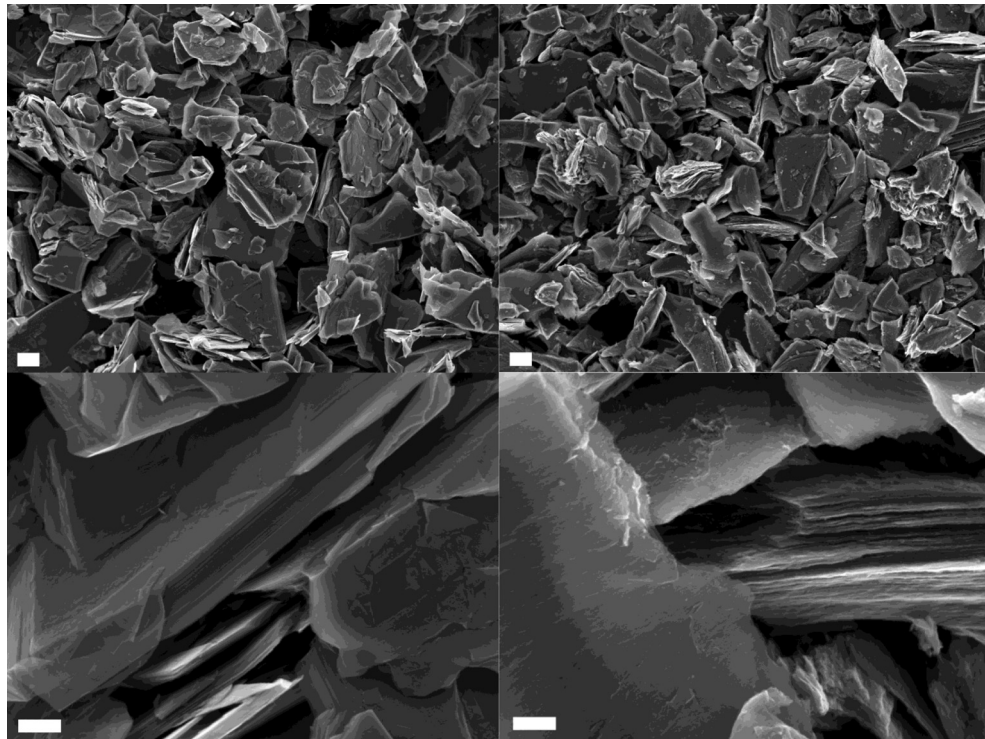


Fig. 1. SEM micrographs of SFG6 (left, graphite) and PeC (right, soft carbon) powder samples. Magnification is 5k (top) and 50k (bottom). The white block represents 1 μm and 200 nm, respectively.

Particle size distributions were extracted using the IRENA tool package [35], using globules form factor (aspect ratio = 1) and maximum entropy algorithm. The total specific surface SSA_{PSD} was obtained by integrating the whole particle surface distribution.

Mesoscopic specific surface $\text{SSA}_{\text{Porod}}$ in $\text{m}^2 \text{ g}^{-1}$ has been extracted from low Q limit using the Porod's law of scattering by sharp interfaces [36,37]:

$$I(\text{cm}^2 \text{ g}^{-1}) = 2\pi(\Delta\rho)^2 \text{SSA}_{\text{Porod}} Q^{-4} \quad (2)$$

The scattering length contrast $\Delta\rho$ was estimated based on the skeleton density, which we measured using a Micromeritics AccuPyc II 1340 He pycnometer.

3. Results and discussion

The SEM micrographs of graphite (SFG6) and soft carbon (PeC) powder are shown in Fig. 1. In contrast to the particle size indicated

in the technical data sheets, a significant difference in terms of size between the two materials is not visible [32,33]. The particles have irregularly shapes with edge length below 10 μm . The layered structure of both materials can be seen in the close-ups. Soft carbon, however, shows a higher roughness compared to graphite. Taking these images into account, the formation of agglomerates could be the reason for the (too) high estimated particle size for soft carbon.

Fig. 2 shows a comparison of the theoretical diffractogram of graphite, calculated with the cell parameters and the atom coordinates and the experimentally measured diffractograms of graphite and soft carbon powder [38]. As shown, the diffractogram of the graphite powder matches very well with the theoretical one. The (002) signal of soft carbon is shifted to smaller 2θ values and is much broader compared to the sharp graphite peaks, indicating the presence of a less crystalline structure. Table 2 reports the lattice plane distance calculated for both graphite and soft carbon as obtained using the experimental 2θ values of the (002) reflection in Bragg's equation. The interlayer distance of lithiated graphite, taken from literature, and the interlayer distance of lithiated soft carbon (as well measured with XRD) are also included on the table [39]. The signal corresponding to the graphene–graphene interlayer distances in pristine and lithiated carbon has different Miller indices due to the different stacking sequence and therefore unit cell dimensions. The lattice plane distance of pristine graphite is

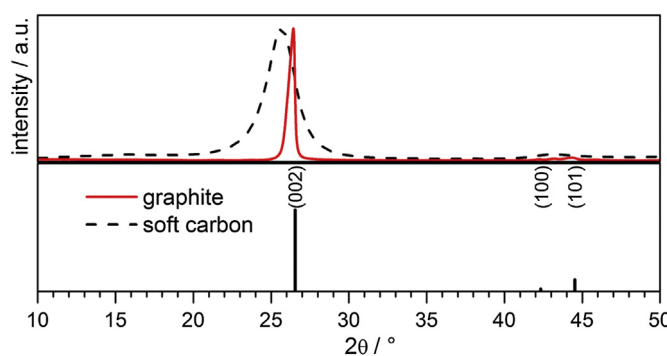


Fig. 2. Powder XRD of PeC and SFG6 and theoretical calculated for graphite.

Table 2
Incident angle and lattice plane distance of the (002)/(001) lattice plane families.

Material	$2\Theta / {}^\circ$	d_{002}/pm	d_{001}/pm
SFG6	26.46	336.8	
PeC	25.85	344.6	
SFG6 (LiC_6)	~		370 [39]
PeC (LiC_9)	24.06		369.8

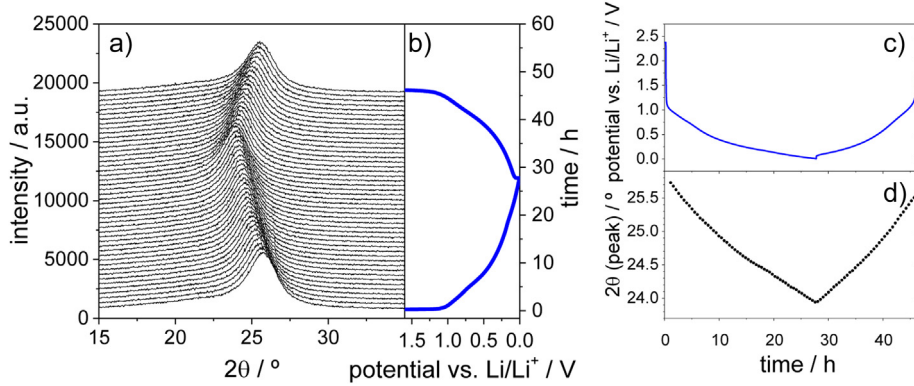


Fig. 3. *In-situ* XRD patterns of PeC during lithium insertion/extraction in the carbon structure (a), potential versus time curve of the *in-situ* experiment (b and c) and 2θ position of the (002) diffraction peak versus time plot (d).

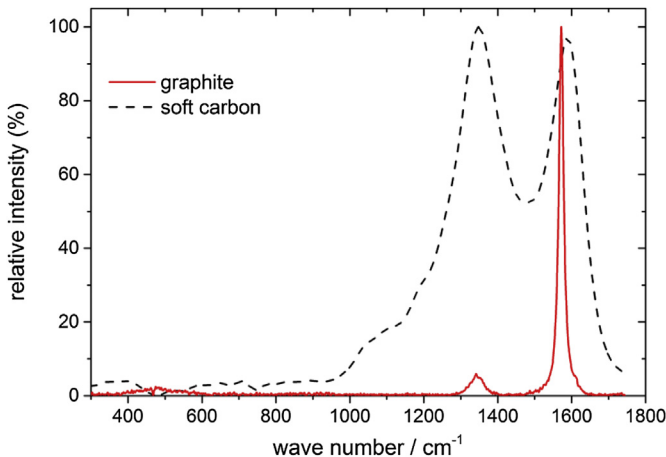


Fig. 4. Raman spectra of PeC and SFG6.

very close to the ideal graphitic value of 335.4 pm. The lattice plane distance of soft carbon is around 10 pm bigger, in the typical range of this material, which lies between the ideal graphite and a hard carbon with a lattice plane distance of at least 380 pm [40]. The fully lithiated soft carbon (250 mAh g⁻¹, corresponding to a composition of LiC₀) has the same (001) interlayer spacing of 370 pm as fully lithiated graphite. However, the relative volume expansion between the pristine and the lithiated material is slightly lower for soft carbon (9% for SFG6, 7% for PeC).

Fig. 3 shows an *in-situ* XRD study performed on a soft carbon based electrode during lithium insertion/extraction. The diffraction angle of the (002) signal of soft carbon varies monotonously with the lithiation degree of the system indicating the insertion and extraction of lithium ions into the carbon structure. Comparing these results with *in-situ* investigations of Dahn et al., it is evident that the peaks for the PeC are thinner (corresponding to a more crystalline material), while the evolution of the peak position of both materials is the same [41]. It is interesting to note that in contrast to *in-situ* XRD measurements of graphitic materials only one peak is present over the total experiment [42,43]. This is a first indication that no staged lithium insertion mechanism is present, as it can be observed for graphites.

Fig. 4 compares the Raman spectra of the two investigated materials. Both of them show the two typical signals for carbonaceous materials: the G-band (*graphene*, corresponding to basal planes/sp² carbon networks) at 1580 cm⁻¹ and the D-band (*disorder*, corresponding to defects and prismatic edges) at 1350 cm⁻¹ [44]. The G-band of graphite is around twenty times bigger compared to the D-band, indicating the presence of crystalline domains and fewer edges. In contrast, both signals have similar intensities in the soft carbon spectrum. The 1:1 ratio between the two bands can be explained by the presence of smaller crystalline domains (decreased G-band) and more crystallite edges (increased D-band) compared to graphite. Although both materials have a similar particle size as shown by SEM, soft carbon appears less crystalline than graphite. Considering this difference, it is reasonable to suppose that lithium ions have more (possible) entrance spots to penetrate the particles in soft carbon compared to graphite.

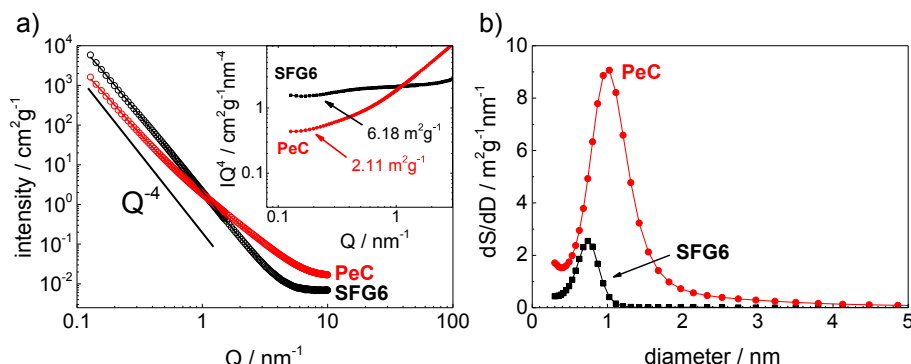


Fig. 5. a) SAXS intensity versus scattering angle of SFG6 (black circles) and PeC (red circles). The solid curved lines are the fit by the size distribution simulation. The thin straight line indicates the Porod scattering in Q^{-4} . Inset: Porod plot of SFG6 (black) and PeC (red). b) Specific surface distribution versus diameter size extracted from SAXS data of graphite (black) and PeC (red). (For interpretation of the references to color in this figure legend, the reader is referred to the web version of this article.)

Table 3

Pycnometer density, SAXS scattering contrast and specific surface areas deduced from SAXS and gas adsorption (BET).

	Pycnometer density/cm ³ g ⁻¹	Scattering contrast $\Delta\rho/\times 10^{-3}$ nm ⁻⁴	SSA from SAXS		SSA _{BET} /m ² g ⁻¹
			Mesopores SSA _{Porod} /m ² g ⁻¹	Total SSA _{PSD} /m ² g ⁻¹	
PeC	2.129 ± 0.003	1.811	2.11	77.9	3.98
SFG6	2.360 ± 0.015	2.007	6.18	18.9	17

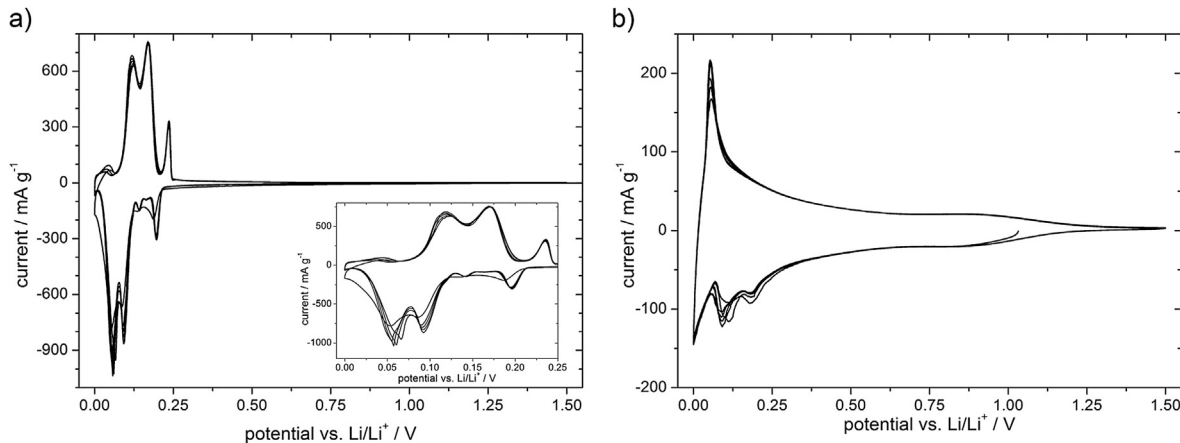


Fig. 6. Cyclic voltammeteries of graphite (a) and soft carbon based anodes (b) performed with a scan rate of 50 $\mu\text{V s}^{-1}$ between 0 and 1.5 V vs. Li/Li⁺.

Fig. 5 compares the SAXS intensity (Fig. 5a) and extracted specific surface distribution dS/dD (Fig. 5b) of PeC and SFG6. Both of them show SAXS intensity that follows the Q⁻⁴ Porod's law (Eq. (2)) in the low Q limit, indicating the presence of large particles (>50 nm according to the lowest Q reached) in accordance with the SEM images. The specific surfaces SSA_{Porod} extracted from the application of Porod's law in this low Q limit are summarized in Table 2 for both samples. They can be reasonably ascribed to the surface area, at mesoscopic scale, of the large particles of PeC and SFG6 seen in the SEM images of Fig. 1. Comparing with the specific surface SSA_{BET} extracted from BET analysis of gas adsorption, we can see that SSA_{Porod} accounts for only part of SSA_{BET} (half for the PeC and one third for the graphite), which indicates the presence of a certain roughness of the particles' surface at smaller (nanometric) scale.

In the case of SFG6 (Fig. 5a), despite a slight increase in intensity around $Q = 0.3\text{--}0.5 \text{ nm}^{-1}$, the fact that the Porod's law applies up to $Q = 3 \text{ nm}^{-1}$ indicates the presence of smooth particles' surface up to the nanometric scale, in accordance with the SEM picture of Fig. 1 bottom left. Above $Q = 3 \text{ nm}^{-1}$ the intensity becomes constant as the background noise level is reached. In the case of PeC (Fig. 5a), the SAXS intensity follows Porod's law only in the low Q limit, while departs clearly from Q⁻⁴ above $Q = 0.2 \text{ nm}^{-1}$. This indicates the presence of roughness of the particles' surface at the nanometric scale, in agreement with SEM images of Fig. 1 bottom right.

In order to interpret quantitatively the deviations of the Porod's law of both samples in terms of specific surface area, a particle size distribution (PSD) analysis of the SAXS data has been performed which allows extracting the surface area distribution dS/dD as reported on Fig. 5b. A significantly higher amount of specific surface at the nanometric and sub-nanometric scale is clearly revealed in PeC compared to SFG6, indicating important roughness of the PeC particle surface at this scale. The total specific surface SSA_{PSD} obtained by integrating the dS/dD distribution over the whole size range is reported in Table 3. While SSA_{PSD} is quite close to SSA_{BET} for SFG6, for PeC it is about twenty times higher than SSA_{BET} and forty times higher than SSA_{Porod}. This discrepancy between gas adsorption and SAXS measurements in the case of PeC can be ascribed to

the fact that SAXS is sensitive to surface roughness down to the atomic scale while gas adsorption is limited by the size of the probe gas molecule. This greater amount of specific surface at the nanometric and subnanometric scale in the case of PeC probably accounts for the presence of a larger amount of crystallite edges at the surface as deduced from Raman measurements.

Summing up the results of SEM, XRD, SAXS and Raman investigations, it appears that graphite and soft carbon, even if they have a similar size, display different microstructural properties. Soft carbon shows a higher interlayer distance in pristine state and an increased fraction of prismatic surfaces. Both factors should favor lithium insertion/charge transfer at increased currents. Nevertheless, it is important to note that also the soft carbon structure has to expand to accommodate the lithium, which would be not the case for hard carbons.

Fig. 6 shows cyclic voltammeteries of graphite (Fig. 6a) and soft carbon based anodes (Fig. 6b). While lithiation of the soft carbon

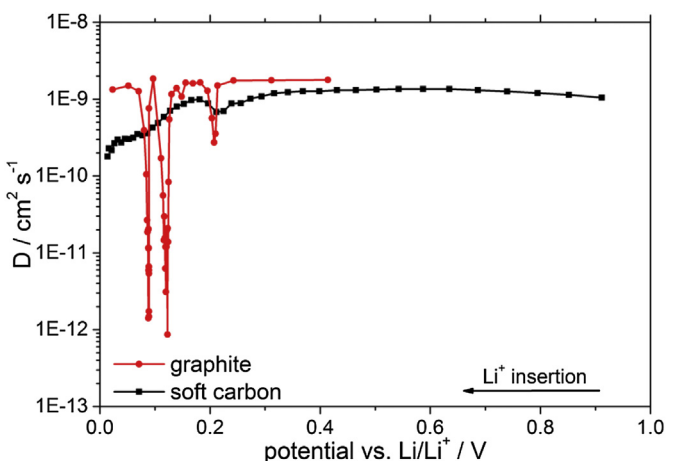


Fig. 7. GITT measurements of graphite and soft carbon based anodes during lithiation.

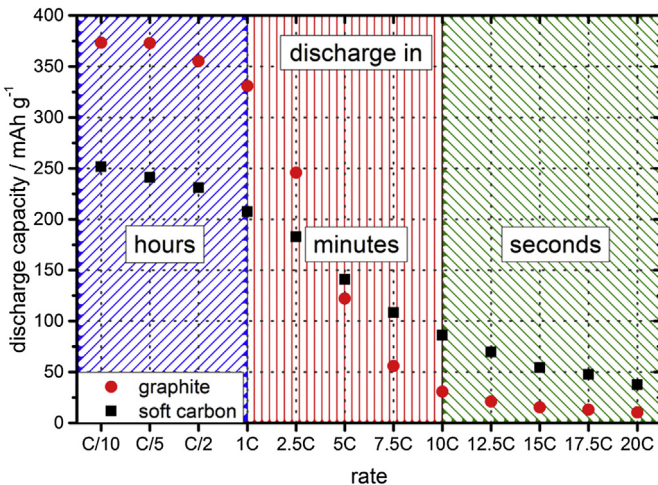


Fig. 8. C-rate test of graphite and soft carbon based anodes between 0 and 1.5 V vs. Li/Li⁺.

begins already at potentials of around 1.25 V vs. Li/Li⁺, lithium is intercalated into the graphite only between 250 and 50 mV vs. Li/Li⁺. Graphite shows distinct intercalation and deintercalation peaks corresponding to the different passed through stages. On the contrary, soft carbon shows only one major lithium-extraction peak

and the insertion signals are much broader und blurred together. The advantages and disadvantages of the broader insertion and extraction range for amorphous carbons will be discussed below in more detail.

Fig. 7 compares the evolution of the lithium diffusion coefficient over the potential for graphite and soft carbon, as obtained via GITT measurement. It is important to remark that in order to obtain reliable results from GITT experiments several requirements have to be fulfilled. Firstly, the electrodes have to be solid and non porous. Secondly, the electrode surface and their shape have to be known. Thirdly and finally, the diffusion has to be the rate determining step [34]. In our study all of these prerequisites are only partially fulfilled. Furthermore, it is important to note that the presence of several two-phase stage regions in graphite may hinder an accurate GITT measurement. We are also aware of the discussions concerning the use, validity and applicability of techniques like GITT or of the Randles–Sevcik equation for electrochemistry of electroactive films [45–47]. Therefore, the values indicated in **Fig. 7** have to be considered as an indication of the variation of the lithium diffusion coefficient over the potential only. Nevertheless, the results can be still analyzed qualitatively and from them reasonable conclusions concerning the general trend of the lithium insertion process can be made. From the figure, it is evident that the lithium insertion in graphite is hindered every time a new intercalation stage is reached (the same apply for the extraction process, not shown here). As shown, at each stage the diffusion coefficient

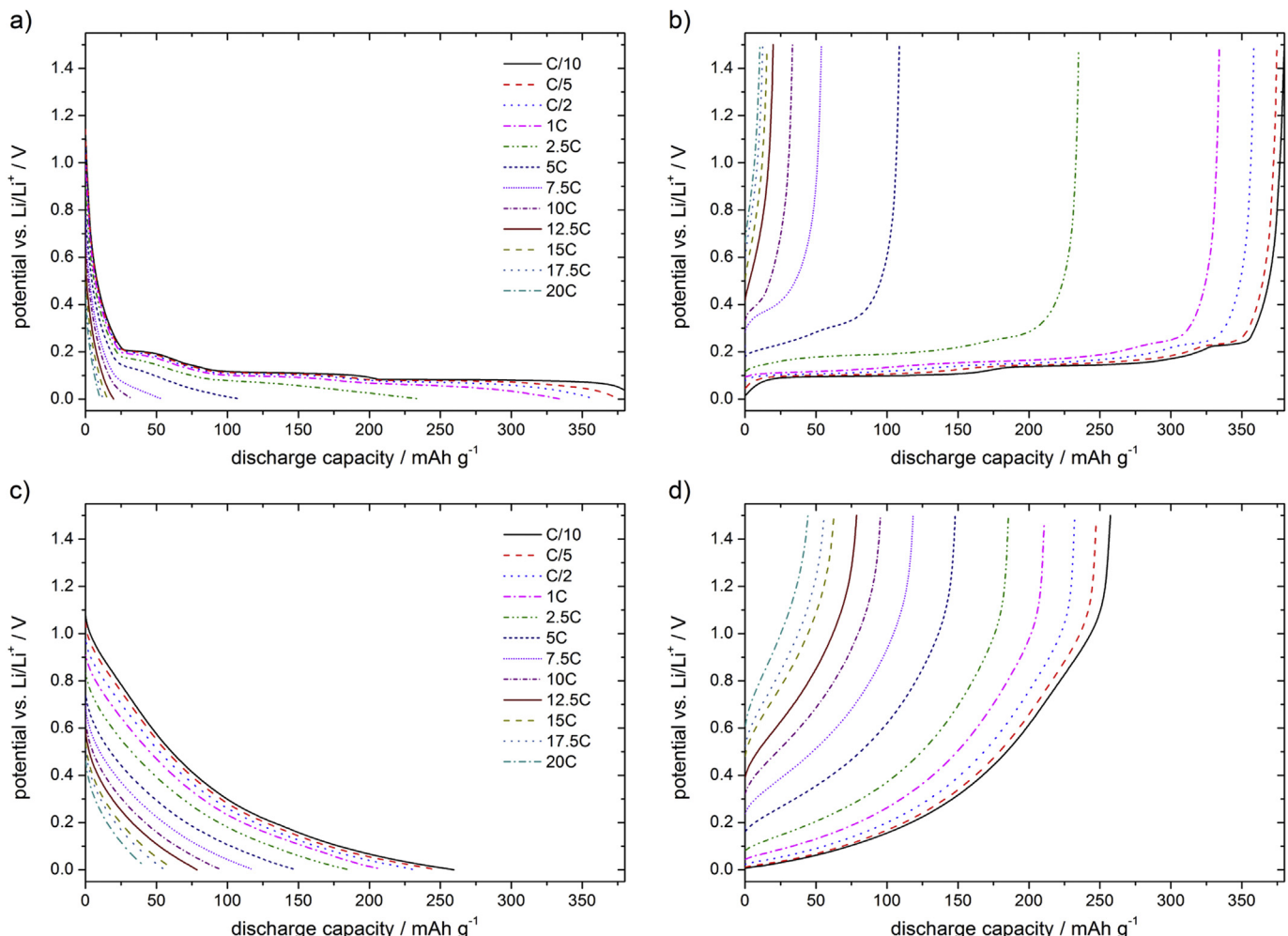


Fig. 9. Lithium insertion (left) and extraction (right) profiles of graphite (a, b) and soft carbon (c, d) based anodes measured at rates from C/10 to 20C.

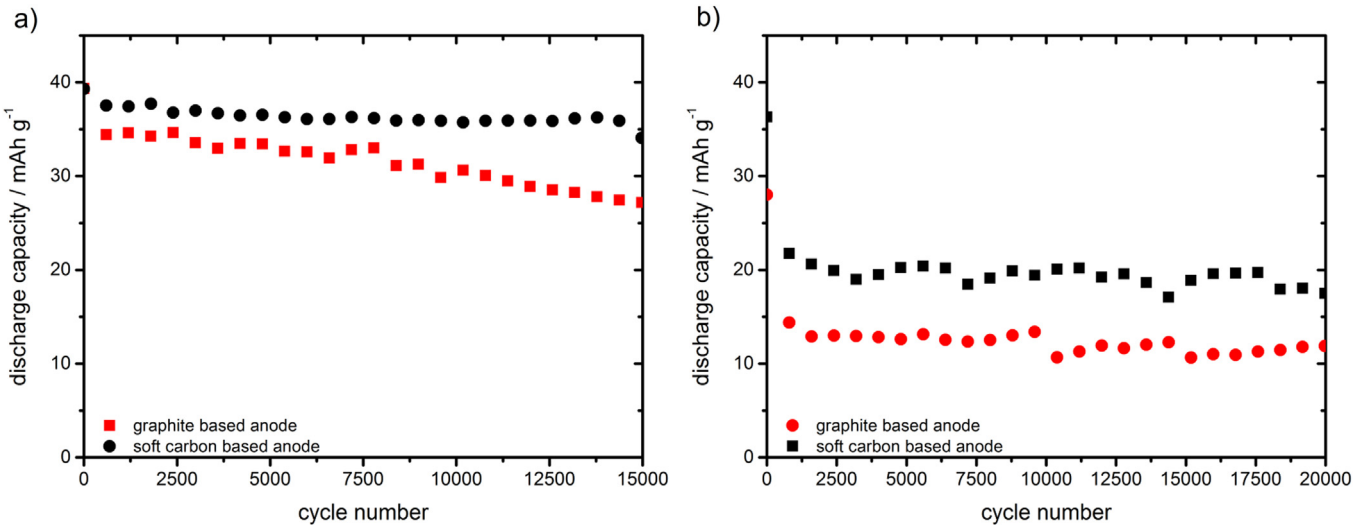


Fig. 10. Long term constant current cycling of graphite/AC and soft carbon/AC based LICs with LP30 as electrolyte cycled at 5C a) and at 15C b) for 15,000 and 20,000 cycles.

drops one up to three orders of magnitude [48,49]. Aurbach et al. explained this behavior by lithium cluster formation between two carbon layers, which traps the diffusion of other lithium ions in the beginning of a new stage [48,49]. Other reasons could be a hindrance in desolvation and charge-transfer, which is, according to Pandolfo et al., one of the main bottlenecks of lithium insertion in graphites [21]. In contrast to graphite, soft carbon does not show significant decreases of the diffusion coefficient over the investigated potential range. The different behavior of the two materials can be explained taking into account the lithium insertion mechanism in soft carbons. No intercalation stages are present and therefore the effects of lithium cluster formation are suppressed. Additionally, also the increased number of prismatic surfaces, which enable a favored desolvation of the lithium ions, might have a non-negligible effect of the lithium insertion process.

The different lithium insertion process occurring in graphite and soft carbon has an important consequence on the capacity of the materials during charge–discharge carried out at high current densities. As shown in Fig. 8, when low C-rates are applied the graphite electrode displays, due to its characteristics, higher capacities compared to soft carbon-based electrode. For example, at C/10 the graphite electrode display a discharge capacity of the theoretical 372 mAh g⁻¹, while the soft carbon of only 250 mAh g⁻¹. However, starting from 5C the soft carbon electrode displays much higher capacity compared to the graphite electrode. At 10C the capacity delivered by the soft carbon electrode (ca. 90 mAh g⁻¹) is more than three times higher than that of graphite (ca. 25 mAh g⁻¹). The different behavior of these two carbonaceous electrodes during charge–discharge at high current densities is well visible on their voltage profiles (Fig. 9). At low C-rates the graphite electrode utilizes all intercalation plateaus corresponding to the insertion–extraction of lithium. At the same C-rate, the soft carbon shows a much more sloped profile. When the C-rate is increased, the plateaus of the graphite electrode are pushed out of the working potential window. The first intercalation plateau is already lost at a rate of 2.5C, the second one is lost at 5C and the third shorter one cannot be reached at 10C anymore (Fig. 9a). On the contrary, the profile of the soft carbon anode does not change so dramatically. The electrode potential is also shifted to lower values when increased rates are applied. However, the consequence of such a shift, due to the slope profile of this material, is much less dramatic than in the case of graphite (Fig. 9c). It is important to notice that the initial coulombic efficiency of graphite is 82%, while

in the case of soft carbon it reaches only 72%. This difference represents a disadvantage related to the use of soft carbon in LIBs. However, as mentioned above, a prelithiation process is always necessary in LICs and therefore, the lower initial efficiency of soft carbon does not represent an obstacle for its introduction in such devices. The coulombic efficiency in further cycling (not shown here) is way above 99% for both anode materials.

Finally, the two investigated anodic materials were used for the realization of LICs. Fig. 10 compares the evolution of the capacity (referred to the total active material) of LICs containing soft carbon and graphite during charge–discharge cycled at 5C and 15C. As shown, the LICs containing the soft carbon display higher capacity

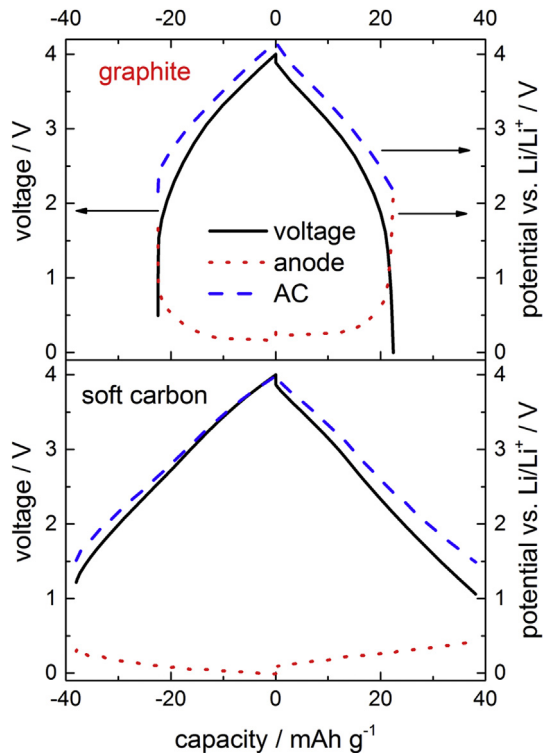


Fig. 11. Potential and voltage profiles of the 15,000th cycle of the graphite (above) and soft carbon (below) based LICs cycled at 5C.

Table 4

Average energy and power values for soft carbon and graphite based LICs at 5C and 15C after 15,000 and 20,000 cycles, respectively.

	Average energy density/ (Wh kg ⁻¹)	Average power density/ (kW kg ⁻¹)
SFG6 5C	63.9	2.1
SFG6 15C	23.7	5
PeC 5C	80.6	1.7
PeC 15C	37.2	4.8

and better cycling stability at both applied C-rates. Considering also the voltage and potential profiles of graphite (Fig. 11 (above)) and soft carbon (Fig. 11 (below)) at the end of cycling, it becomes clear that the increased capacity of the soft carbon based system is originated by the potential profile of this material. In both devices, the anodes potential was not fully utilized. Nevertheless, as shown before, the effect of this is more severe in graphite than in soft carbon. As a consequence of the shift of the anode potential, the potential window of the AC positive electrode becomes narrower over cycling and the cut-off criterion is reached earlier.

The energy and power densities of the two investigated LICs are reported in Table 4. These values are calculated according to literature [22]. As shown, while the power of these devices is comparable, the energy of the LIC containing the soft carbon anode is higher than that of the graphite-based LIC. Fig. 12 compares the accumulated energy density versus the discharge time/capacity of the two devices as obtained during a discharge carried out at 5C. As shown in this figure, when an identical current is applied to these devices, the LIC containing graphite is completely discharged much earlier (110 s vs. 175 s for graphite and soft carbon, respectively). As illustrated in Fig. 12 (below), where the discharged voltage profiles

of the two LICs are compared, the different discharge time is mainly related to the anodes (see also Fig. 11). As indicated above, the graphite electrode displays a lower capacity than the soft carbon based electrode at 5C. As a consequence of this difference, the soft carbon LIC delivers around 20% of energy more than the graphite-based LIC. When a C-rate of 15C is applied, the difference between the two devices becomes more significant and a LIC containing the soft carbon delivers 35% more energy than the one having graphite as anode.

4. Conclusion

In this paper we showed that soft carbon appears more suitable for application on LICs compared to graphite. While in graphite the lithium insertion is hindered every time a new intercalation stage is reached, in soft carbon the lithium insertion process does not show significant decrease over the used potential. This difference, caused by the different structural and microstructural properties of these carbonaceous materials, has dramatic consequences on the capacity retention of these carbons during the high rates typically used in LIC. When a current density corresponding to 5C is applied, soft carbon-based LICs deliver around 20% of energy more than the graphite-based LIC. When the rate is increased to 15C, this difference becomes more significant, and a LIC containing the soft carbon delivers 35% more energy than the one having graphite as anode.

Acknowledgment

The authors wish to thank the University of Münster, the Ministry of Innovation, Science and Research of North Rhine-Westphalia (MIWF) within the project “Superkondensator und Lithium-Ionen-Hybrid-Superkondensatoren auf der Basis ionischer Flüssigkeiten, EVONIK (within the project EvoCarb) and the Bundesministerium für Bildung und Forschung (BMBF) within the project IES (contract number 03EK3010) for the financial support. J.S., D.S. and M.C.C. wish to acknowledge financial support by the Departamento de Desarrollo Económico y Competitividad of the Gobierno Vasco. We gratefully appreciated the supply of materials by Norit Activated Carbon Holding (AC) and TIMCAL (PC-40OC, SFG6 and Super C65).

References

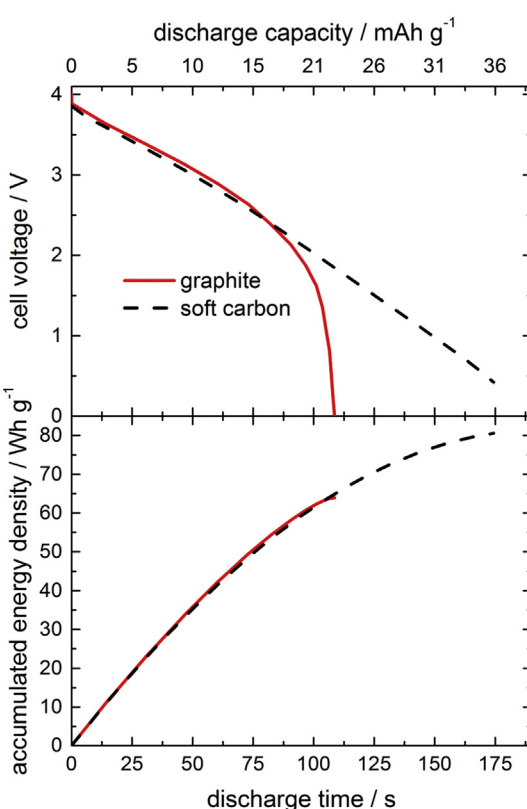


Fig. 12. Cell voltage (above) and accumulated energy density (below) of the graphite and the soft carbon based LICs cycled at 5C versus discharge time/capacity.

- [1] J.P. Zheng, J. Electrochem. Soc. 152 (2005) A1864.
- [2] G.G. Amatucci, F. Badway, A.D. Pasquier, T. Zheng, J. Electrochem. Soc. 148 (2001) A930.
- [3] H. Li, L. Cheng, Y. Xia, Electrochim. Solid-State Lett. 8 (2005) A433.
- [4] R. Vasanthi, D. Kalpana, N. Renganathan, J. Solid State Electrochem. 12 (2008) 961.
- [5] J.P. Zheng, J. Electrochem. Soc. 150 (2003) A484.
- [6] J.P. Zheng, J. Electrochem. Soc. 156 (2009) A500.
- [7] D. Cericola, P. Novák, A. Wokaun, R. Kötz, J. Power Sources 196 (2011) 10305.
- [8] Y. Huai, X. Hu, Z. Lin, Z. Deng, J. Suo, Mater. Chem. Phys. 113 (2009) 962.
- [9] C. Hong Soo, K. TaeHoon, I. Ji Hyuk, P. Chong Rae, Nanotechnology 22 (2011) 405402.
- [10] C.M. Ionica-Bousquet, D. Muñoz-Rojas, W.J. Casteel Jr., R.M. Pearlstein, G.G. Kumar, G.P. Pez, M.R. Palacín, J. Power Sources 196 (2011) 1626.
- [11] J. Ni, L. Yang, H. Wang, L. Gao, J. Solid State Electrochem. 16 (2012) 2791.
- [12] H.-G. Jung, N. Venugopal, B. Scrosati, Y.-K. Sun, J. Power Sources 221 (2013) 266.
- [13] J.J. Yang, H.I. Kim, Y.-J. Yuk, H.-J. Kim, S.-G. Park, J. Electrochim. Sci. Technol. 1 (2008) 63.
- [14] V. Khomenko, E. Raymundo-Piñero, F. Béguin, J. Power Sources 177 (2008) 643.
- [15] C. Decaux, G. Lota, E. Raymundo-Piñero, E. Frackowiak, F. Béguin, Electrochim. Acta 86 (2012) 282.
- [16] W.J. Cao, J.P. Zheng, J. Power Sources 213 (2012) 180.
- [17] JM energy corporation, http://www.avususergroups.org/tfug_pdfs/2009_2banas.pdf (last visited 27.01.2014).
- [18] S.R. Sivakkumar, A.S. Milev, A.G. Pandolfo, Electrochim. Acta 56 (2011) 9700.
- [19] S.R. Sivakkumar, A.G. Pandolfo, Electrochim. Acta 65 (2012) 280.
- [20] J.-H. Kim, J.-S. Kim, Y.-G. Lim, J.-G. Lee, Y.-J. Kim, J. Power Sources 196 (2011) 10490.

- [21] S.R. Sivakkumar, J.Y. Nerkar, A.G. Pandolfo, *Electrochim. Acta* 55 (2010) 3330.
- [22] M. Schroeder, M. Winter, S. Passerini, A. Balducci, *J. Electrochem. Soc.* 159 (2012) A1240.
- [23] M. Schroeder, P. Isken, M. Winter, S. Passerini, A. Lex-Balducci, A. Balducci, *J. Electrochem. Soc.* 160 (2013) A1753.
- [24] M. Schroeder, M. Winter, S. Passerini, A. Balducci, *J. Power Sources* 238 (2013) 388.
- [25] W.J. Cao, J.P. Zheng, *J. Electrochem. Soc.* 160 (2013) A1572.
- [26] C. Del Río, M.C. Ojeda, J.L. Acosta, *J. Appl. Polym. Sci.* 74 (1999) 1003.
- [27] T.D. Tran, D.J. Derwin, P. Zaleski, X. Song, K. Kinoshita, *J. Power Sources* 81–82 (1999) 296.
- [28] W. Jiang, T. Tran, X. Song, K. Kinoshita, *J. Power Sources* 85 (2000) 261.
- [29] R. Alcantara, J.M.J. Mateos, J.L. Tirado, *J. Electrochem. Soc.* 149 (2002) A201.
- [30] Y. Sato, K. Nagayama, Y. Sato, T. Takamura, *J. Power Sources* 189 (2009) 490.
- [31] Y. Nishi, *Chem. Rec.* 1 (2001) 406.
- [32] Technical data sheet – Timrex PC40-OC, Timcal Ltd., 2008.
- [33] Technical Data Sheet – Timrex SFG6, Timcal Ltd., 2006.
- [34] W. Weppner, R.A. Huggins, *J. Electrochem. Soc.* 124 (1977) 1569.
- [35] J. Ilavsky, P.R. Jemian, *J. Appl. Crystallogr.* 42 (2009) 347.
- [36] G. Porod, *Kolloid-Zeitschrift* 124 (1951) 83.
- [37] G. Porod, in: O. Glatter, O. Kratky (Eds.), *Small Angle X-ray Scattering*, Academic Press, London, 1982.
- [38] A. Bosak, M. Krisch, M. Mohr, J. Maultzsch, C. Thomsen, *Phys. Rev. B* 75 (2007) 153408.
- [39] X.Y. Song, K. Kinoshita, T.D. Tran, *J. Electrochem. Soc.* 143 (1996) L120.
- [40] M. Winter, K.-C. Moeller, J.O. Besenhard, in: G.-A. Nazri, G. Pistoia (Eds.), *Lithium Batteries Science and Technology*, Kluwer Academic Publisher, Boston, 2004.
- [41] D.A. Stevens, J.R. Dahn, *J. Electrochem. Soc.* 148 (2001) A803.
- [42] J.R. Dahn, *Phys. Rev. B* 44 (1991) 9170.
- [43] J. Park, S.S. Park, Y.S. Won, *Electrochim. Acta* 107 (2013) 467.
- [44] M.A. Pimenta, G. Dresselhaus, M.S. Dresselhaus, L.G. Cancado, A. Jorio, R. Saito, *Phys. Chem. Chem. Phys.* 9 (2007) 1276.
- [45] H. Xia, L. Lu, M.O. Lai, *Electrochim. Acta* 54 (2009) 5986.
- [46] A. Eftekhari, *Electrochim. Acta* 55 (2010) 3434.
- [47] L. Lu, *Electrochim. Acta* 55 (2010) 3435.
- [48] M.D. Levi, E.A. Levi, D. Aurbach, *J. Electroanal. Chem.* 421 (1997) 89.
- [49] E. Markevich, M.D. Levi, D. Aurbach, *J. Electroanal. Chem.* 580 (2005) 231.